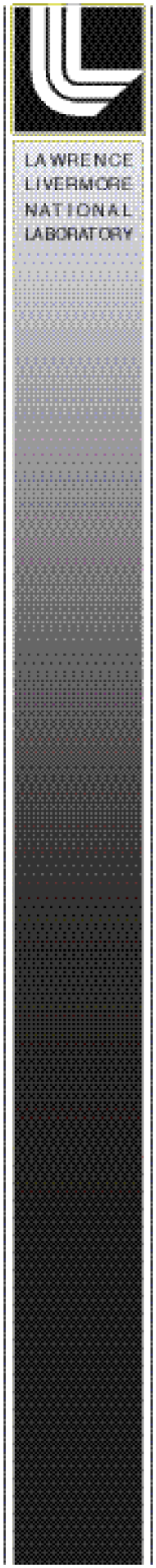

LLNL-TR-462751

Modifications and applications of the HERMES model: June-October 2010

John E. Reaugh

November 16, 2010

Disclaimer

This work performed under the auspices of the U.S. Department of Energy by Lawrence Livermore National Laboratory under Contract DE-AC52-07NA27344.

Modifications and applications of the HERMES model: June-October 2010

John E. Reaugh
November 16, 2010

1. Introduction

The HERMES (High Explosive Response to MEchanical Stimulus) model has been developed [1-3] to describe the response of energetic materials to low-velocity mechanical stimulus, referred to as HEVR (High Explosive Violent Response) or BVR (Burn to Violent Reaction). For tests performed with an HMX-based UK explosive, at sample sizes less than 200 g, the response was sometimes an explosion, but was not observed to be a detonation. The distinction between explosion and detonation can be important in assessing the effects of the HE response on nearby structures. A detonation proceeds as a supersonic shock wave supported by the release of energy that accompanies the transition from solid to high-pressure gas. For military high explosives, the shock wave velocity generally exceeds 7 km/s, and the pressure behind the shock wave generally exceeds 30 GPa. A kilogram of explosive would be converted to gas in 10 to 15 microseconds. An HEVR explosion proceeds much more slowly. Much of the explosive remains unreacted after the event. Peak pressures have been measured and calculated at less than 1 GPa, and the time for the portion of the solid that does react to form gas is about a millisecond. The explosion will, however, launch the confinement to a velocity that depends on the confinement mass, the mass of explosive converted, and the time required to form gas products. In many tests, the air blast signal and confinement velocity are comparable to those measured when an amount of explosive equal to that which is converted in an HEVR is deliberately detonated in the comparable confinement. The number of confinement fragments from an HEVR is much less than from the comparable detonation.

The HERMES model comprises several submodels including a constitutive model for strength, a model for damage that includes the creation of porosity and surface area through fragmentation, an ignition model, an ignition front propagation model, and a model for burning after ignition. We have used HERMES in computer simulations of US and UK variants of the Steven Test [4]. We have recently improved some of the submodels, and report those developments here, as well as the results of some additional applications.

2. Pressure and strain dependence of the flow stress at constant strain rate

The new calculation of the pressure- and strain- dependent strength (version 67e) proceeds as follows. We first calculate the parameter Ω, which is a measure of damage.

$$\Omega = \frac{D \max(0, \varphi_{old} - \varphi_{cr})}{1 + D \max(0, \varphi_{old} - \varphi_{cr})} \qquad (1)$$

where φ_{old} is the previous value of the porosity, D and φ_{cr} are parameters. The strain hardening parameter δ is calculated

$$\delta = \frac{\varepsilon_p}{\varepsilon_p + \varepsilon_h}. \tag{2}$$

where ε_h, is a parameter and ε_p is the plastic strain. For a given strain-rate, the strain-rate parameter R is calculated by

$$R = \left(1 + \frac{\dot{\varepsilon}_p}{\dot{\varepsilon}_0}\right)^{ep} \tag{3}$$

where ep and $\dot{\varepsilon}_0$ are parameters.

The strength of fully damaged material (residual strength) is given by

$$Y_r = RY_0\left(\frac{A_r}{Y_0} + B_r \frac{p}{RY_0}\right) \tag{4}$$

where A_r, B_r, and Y_0 are parameters. The residual strength is constrained not to exceed the intact strength. For geologic materials, the parameter A_r is taken to be zero to represent cohesionless soils and broken rock [5]. Here we let the parameter A_r be larger than zero to represent the observed rate-dependent residual strength of explosive at (nearly) zero pressure. The strength of the intact material is given by

$$Y_i = RY_0\sqrt{s + m\frac{p}{RY_0} + (m/6)^2} - (m/6) \tag{5}$$

for $p \geq 0$. Here s and m are parameters and s generally takes the value one. For p < 0, a straight line interpolation between the uniaxial tensile strength to Y_i (0) is made and extended to the pressure intercept at zero strength.

$$Y_i(p < 0) = Y_i(0) + \frac{3[Y_i(0) - Y_t]}{Y_t} p \tag{6}$$

where Y_t is the characteristic uniaxial tensile strength and is specified to be equal to $b_{ten}Y_0$ where b_{ten} is an input parameter between zero and one. The floor value of Y_i is zero. The intact strength is modified by multiplying by the strain hardening term f_e.

$$f_e = \delta + C(1 - \delta) \tag{7}$$

where C is a parameter between zero and one. The flow stress is then given by

$$Y = Y_i f_e(1 - \Omega) + Y_r\Omega. \tag{8}$$

This is the flow stress when two of the three principal stresses are equal and are less compressive than the third. If the Mohr-Coulomb modification is desired, the flow stress is further modified by the appropriate factor given in section 3. If not, the calculated flow stress is not further modified.

The new calculation of the pressure dependence of strength is explicit in pressure, and so does not require iteration as did the previous version. As a result, simulations of the Steven test using the new calculation were observed to require only 60% of the computer time needed by the previous pressure dependent calculation. In addition, the use of residual strength improves the fit to the experimental data. Figures 1 and 2 show the old fit and the new fit to experimental data.

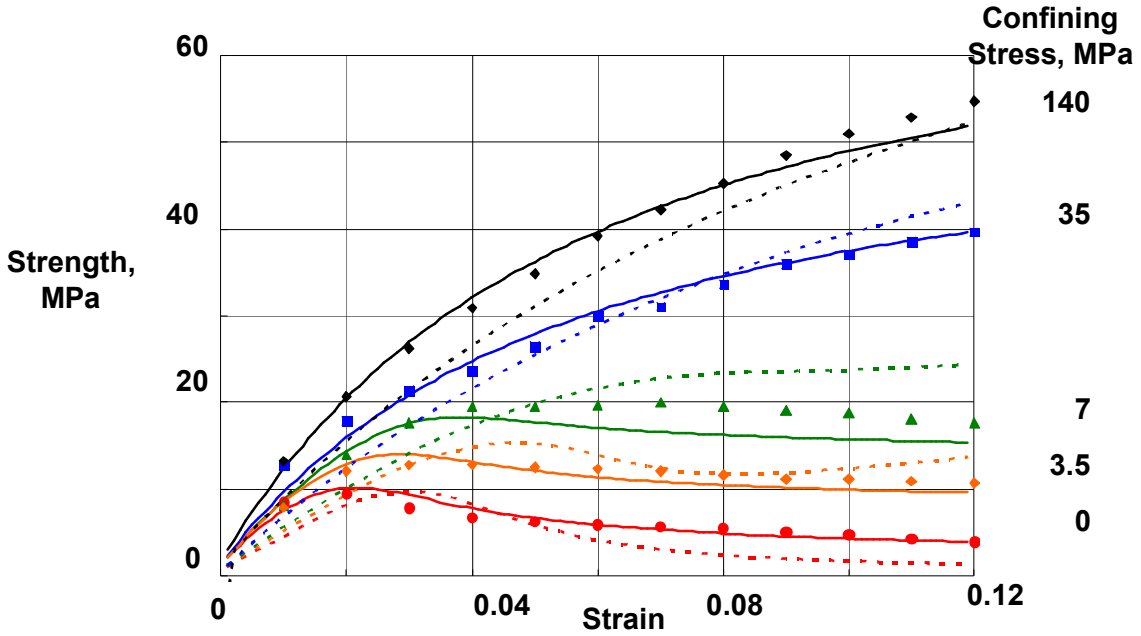

Figure 1. New model (solid) and old model (dash) fit to quasistatic triax test data (symbols) for various confining stresses.

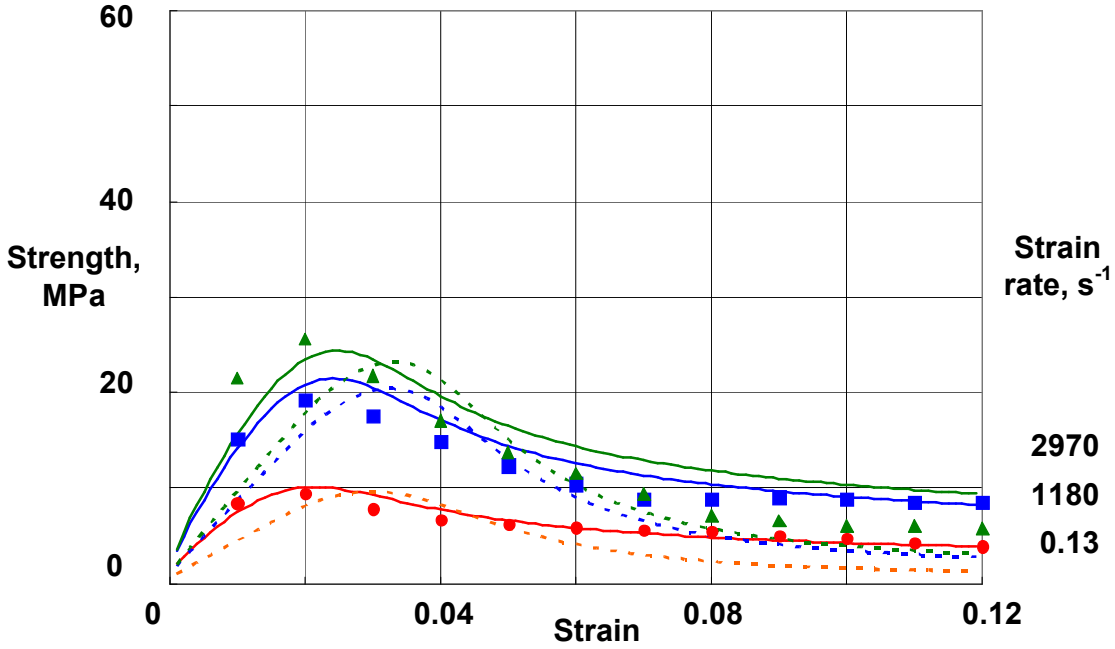

Figure 2. New model (solid) and old model (dash) fit to dynamic split Hopkinson bar and quasistatic uniaxial compression data (symbols) at various strain rates.

3. The Mohr-Coulomb model

For metals and clays, the von Mises criterion for strength is widely used. In principal stress space, with axes (σ_1, σ_2, σ_3), the von Mises criterion is a right circular cylinder whose axis is the principal diagonal. A cross-section normal to that cylinder is a circle, whose radius is the equivalent stress. See Figure 3. Although experiments to probe the yield surface are difficult, they have been done in a few instances, and for metals and clays, the yield surface can be nearly circular. Some tests with an aluminium alloy [6] , however, have shown that even for metals the equivalent strength in shear may not lie on the circle scaled to compression or tension. We are ignoring here such effects as kinematic hardening, whereby the circle does not expand with increasing plastic strain, but rather translates in the direction of straining.

In contrast, for geologic and granular materials, the Mohr-Coulomb criterion is widely used [3]. The condition for that criterion is

$$\frac{\sigma_c - \sigma_t}{2} = f_1\left(\frac{\sigma_c + \sigma_t}{2}\right), \tag{9}$$

where σ_c is the most compressive principal stress and σ_t is the most tensile principal stress. In this formulation, compressive stresses are positive. Most hydrodynamics codes follow the convention described by Wilkins [7] so that the principal stresses and stress deviators are positive in tension, and pressure is positive in compression. In terms of the principal stress deviators ordered algebraically, we have

$$s_1 \geq s_2 \geq s_3, \quad s_1 + s_2 + s_3 = 0. \tag{10}$$

The Mohr-Coulomb criterion is rewritten for the hydrocode convention as

$$\frac{s_1 - s_3}{2} = A + B\left(p - \frac{s_1 + s_3}{2}\right), \tag{11}$$

where we have made the general functional dependence a (locally) linear one.

For our explosive, the data for pressure, strain-, and strain-rate dependent flow strength were taken in either uniaxial or triaxial compression. In uniaxial compression, the lateral stress is zero, whereas in triaxial compression, the lateral stress is compressive. In either case, two of the three principal stresses are equal and less compressive than the third (axial) component. It is therefore convenient to make the basis for the model the equivalent stress in compression, so that

$$Y_c = f_2(p). \tag{13}$$

It is convenient to express other states of stress by the parameter ξ where

$$s_2 = \xi\, s_1. \tag{14}$$

Since we use the radial return method [7] for reducing the stress tensor from the elastic trial state to the yield surface, the parameter, ξ can be evaluated from the elastic trial state before the flow stress is calculated. For uniaxial compression, $\xi = 1$. For uniaxial tension, $\xi = -1/2$. In shear, $\xi = 0$. In uniaxial compression, Eq. 11 can be written

$$\frac{3s_1}{2} = A + B\left(p + s_1/2\right). \tag{15}$$

We then evaluate the yield stress in compression as

$$Y_c = \sqrt{\tfrac{3}{2}(s_1^2 + s_2^2 + s_3^2)} = 3s_1, \tag{16}$$

So that Eq. 11 becomes

$$\frac{Y_c}{2} = A + B\left(p + \frac{Y_c}{6}\right). \tag{17}$$

We evaluate B from Eq. 17 by calculating the derivative of the yield surface (Eq. 13) .

$$B = \frac{f_2^{'}}{2 + f_2^{'}/3}\ , \tag{18}$$

where $f_2^{'}$ is the pressure derivative of f_2. At present (version 67e) we are using an expedient function $A_r \exp(-p/Y_0)$ for the pressure derivative (see Eq. 4). We found that the discontinuous change in the pressure derivative where the residual strength is limited by the intact strength led to a discontinuous change in the slope , B, and a discontinuous change to the calculated strength. This prevented convergence when calculating the triax test in extension, where the lateral stresses are more compressive than the axial stress, using Newton iteration. A more satisfactory solution would be to force the residual strength to approach the intact strength gradually as a function of pressure. This has not been implemented.

We evaluate Eq. 3 for the general value of ξ to obtain

$$(1 + \xi/2)s_1 = A + Bp + B\xi\ s_1/2, \tag{19}$$

We use Eq. 17 to evaluate (A+Bp) in terms of Y_c, and note that

$$Y_\xi = \sqrt{3(1 + \xi + \xi^2)}s_1. \tag{20}$$

In terms of the compressive yield stress,

$$Y_\xi = \frac{\sqrt{3(1 + \xi + \xi^2)}(1 - B/3)}{2 + (1 - B)\xi} Y_c. \tag{21}$$

The intersection of the yield surface with the plane perpendicular to the main diagonal or pressure axis, $\sigma_1 = \sigma_2 = \sigma_3$, is shown in Figure 3 for three values of $f_2^{'}$. The extreme value of three is the largest possible value, and corresponds to a friction angle of 90^o where B takes the value one. The slope of one (B = 0.43) is typical of rocks and soils. The value zero corresponds to no pressure dependence, and for that case the yield surface is equivalent to the Tresca condition [6]. The importance for our work is that the equivalent strength in pure shear is reduced relative to that in compression from 0.866 for no pressure dependence to 0.577 for the pressure derivative equal to three.

We have implemented this model as a user option (version 67e) and applied it to the calculation of the residual dent in the UK modification of the Steven test [4]. At 70 m/s, the (extrapolated) dent obtained in the test is about 12 mm. The standard model uses the von Mises “circle.” The calculation with the new fit, and a reduced value of the Teflon strength of 30 MPa, results in calculated dent of 11.7 mm. This is larger than the previously reported value of 10.2 mm [4]. The measured strength of Teflon at relatively high strain rates is 30 MPa [11]. When we used 100 MPa Teflon strength as described in [4], but with the new fit, the calculated dent was 10.6 mm. Most of the difference is due to reduced strength of the Teflon, which permits a larger expansion of the explosive in the steel confinement. The remainder of the difference is due to the decreased residual strength of the explosive with the new fit. When the Mohr-Coulomb option is used with

the 30 MPa strength of Teflon, the calculated dent is 12.2 mm. The same value was obtained whether or not the possibility of discontinuous change in strength was present. Apparently most of the sample is in shear or triaxial compression. The calculated dents with and without the Mohr-Coulomb option are shown in Figure 4.

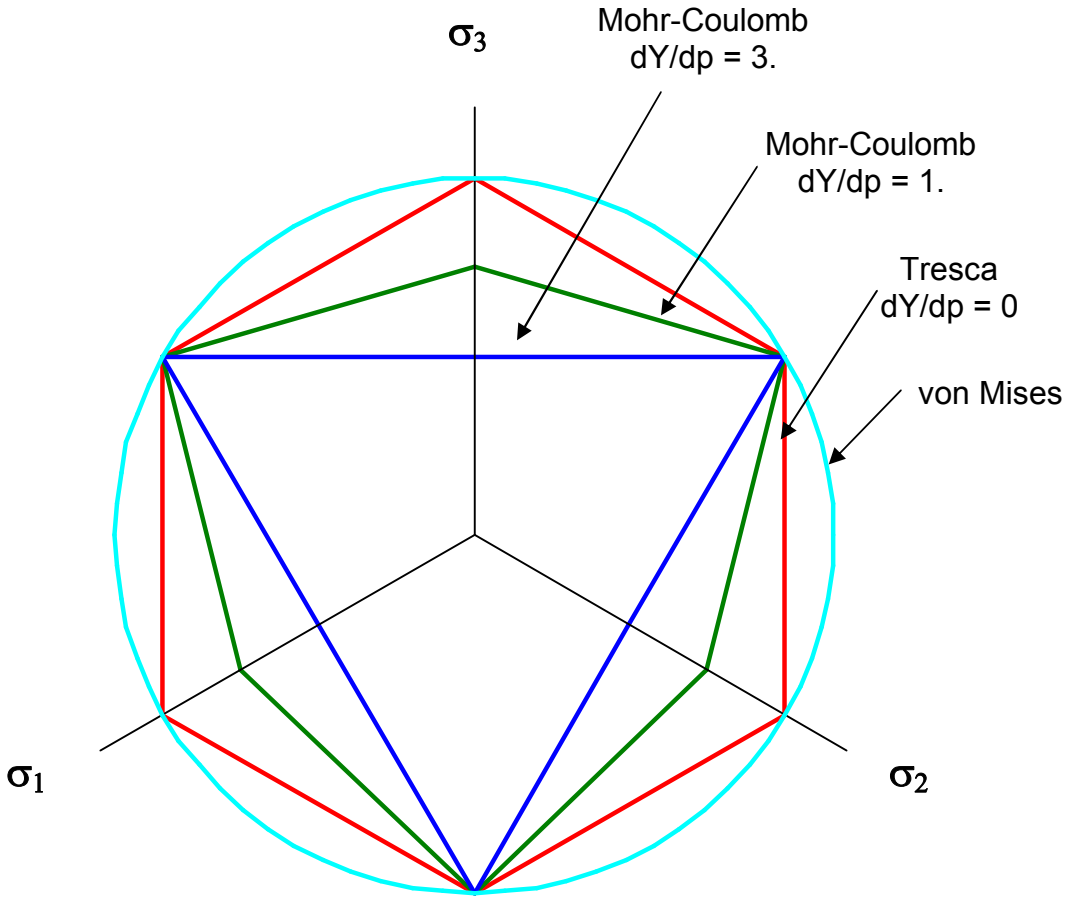

Figure 3. Intersection of the yield surface with a plane normal to the pressure axis. All surfaces are normalized to have the same value in triaxial compression. The three axes (thin black lines) are the three principal stresses. In this figure, the principal stresses are not ordered.

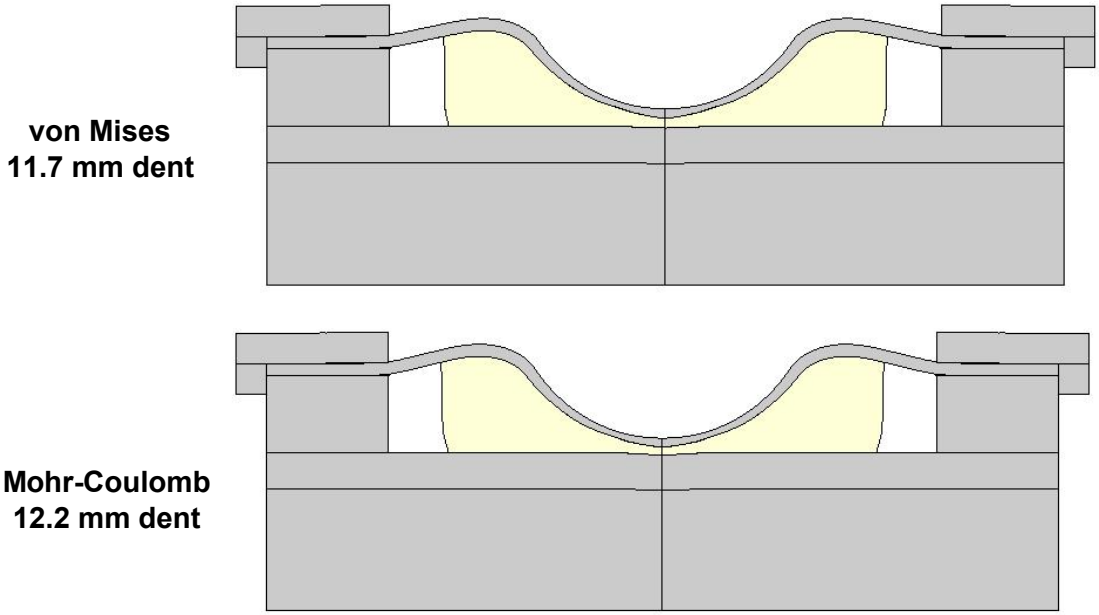

Figure 4. Calculated dents in the UK Steven test with (bottom) and without (top) the Mohr-Coulomb option.

4. Calculation of volume

The volume strain increment is taken to be the sum of the strain increments on the principal diagonal of the strain matrix:

$$\frac{dV}{V} = d\varepsilon_{xx} + d\varepsilon_{yy} + d\varepsilon_{zz} \tag{22}$$

We assume that the strain rate is constant over the time step, *dt.* Then the volume can be calculated by simple integration.

$$\frac{dV}{Vdt} = const = \xi$$

$$\log V_{n+1} - \log V_n = \xi (t_{n+1} - t_n) \tag{23}$$

$$V_{n+1} = V_n \exp(\xi\, dt)$$

The previous method,

$$V_{n+1} = V_n \frac{1 + \xi\, dt/2}{1 - \xi\, dt/2} \tag{24}$$

is accurate enough for small strain increment, but quite poor for large increments. Most hydrocodes have an additional limit on the time step so that the volume change is small enough that the two-step energy iteration is accurate. This is roughly similar to the time step limitation imposed by the artificial viscosity calculation, although imposed both in compression and expansion. It is a limit to the volume change of 4 % in any computational step. LS DYNA apparently does not impose this limit on the time step.

5. Partition of artificial viscosity

We calculate the effect of artificial viscosity on the energy equation in the following way. The energy increment for the element is given by

$$-de = (p+q)dv \tag{25}$$

where de is the specific energy increment, p is pressure, q is artificial viscosity, and dv is the specific volume increment. We express the pressure p as the volume fraction weighted sum of the gas and solid pressures [2], and assume that the artificial viscosity q is apportioned into a gas part and a matrix part.

$$-de = \left(\phi_g p_g + \phi_s p_s + q_g + q_m\right)dv \tag{26}$$

where φ is the volume fraction of gas or solid, and the sum of the volume fractions is one.

$$-de = \left(\phi_g p_g + q_g\right)dv + \phi_s\left(p_g + p_{mm}/\phi_s + q_m\right)dv \tag{27}$$

where we have used the condition for pressure equilibrium [2]

$$p_s = p_g + p_m = p_g + p_{mm}/\phi_s \tag{28}$$

where p_m is the matrix pressure and p_{mm} is the macroscopic matrix pressure. We express dv by its constituent parts

$$dv = \lambda dv_g + (1-\lambda)dv_s \tag{29}$$

where λ is the mass fraction of gas. Collecting terms,

$$-de = \lambda(p_g + q_g)dv_g + (1-\lambda)(p_{mm} + q_m)dv_m + (1-\lambda)(p_g + q_g)dv_s, \tag{30}$$

where we have used the definition of the matrix volume

$$v_m = v/(1-\lambda). \tag{31}$$

Using the equation of pressure equilibrium again, we recognize

$$-de = -\lambda de_g - (1-\lambda)de_m - (1-\lambda)de_s \tag{32}$$

provided that we define

$$-de_s = (p_s - p_{mm}/\phi_s + q_g)dv_s. \tag{33}$$

This method will conserve energy for any partition of artificial viscosity, as long as

$$q = q_g + q_m. \tag{34}$$

We have chosen

$$q_g = f_g q = (p_g/p)q \tag{35}$$

as long as $p > 0$ and $f_g = 0$ otherwise. We note that our method does not result in each of the constituents on their respective Hugoniots as the result of a single shock. This is consistent with the mesoscale view where pressure equilibrium for dissimilar constituents is achieved by multiple shocks and rarefactions.

6. Interface friction, boundary layers, and ignition criteria

The limited number of parametric studies that has been performed for the UK Steven test geometry [3, 4] has demonstrated that the friction coefficient plays a major role in strain localization. Our ignition criterion, which weights both shear strain and the normal stress on the plane of maximum shear, is sensitive to the localization that friction introduces. As a result, the friction coefficient plays a major role in our model's assessment of ignition. We sought to study this interaction computationally in isolation from other complicating factors, such as the strength and compliance of the explosive confinement. To this end, we used the conceptually simple geometry of crushing a disk of

explosive between a falling mass (drop hammer) and a stationary anvil. We took as nominal values a drop height of 0.4 m with drop hammer mass 5 kg and anvil mass 12 kg. The steel drop hammer cylinder has diameter 120 mm and height 60 mm. The anvil is 160mm by 80 mm height. The anvil rests on an unyielding surface. Generally speaking this is the geometry analyzed in [9]. We used a sample volume of 0.2 cm^3 (10 mm diameter and 2.5 mm height) and compressive strength 200 MPa. In absorbing the kinetic energy of the drop hammer, the sample disk is crushed to nearly half its original thickness in the absence of friction. As a result, the mesh is not greatly distorted overall, so the calculation completes easily and accurately. This is a higher strength than is typical for plastic bonded explosives. This is also a much larger volume than is typically used in small scale safety testing. There the sample volume is about a tenth of ours, so that severe deformation is expected, and ignition occurs. In our geometry (by design) we do not expect severe distortion, nor do we expect that the ignition criterion would be met.

Our first set of computer simulations used a constant yield stress of 200 MPa, and a friction coefficient of 0.4, which is the value measured by Hofmann [12] for the friction coefficient between steel and LX-04, an LLNL explosive that is 85% by weight HMX and 15% Viton binder. For these simulations, no limit was placed on the retarding stress, as per the analyses of [9]. This is in contrast to the analyses of Ball [8] where the limit stress would have been set to 115 MPa, the shear stress at yield in pure shear. In our simulations, then, the disk sticks over the inner two-thirds of its surface. At the outer periphery, a portion of the outer (curved) surface of the disk folds over to contact both the falling mass and the stationary anvil during the deformation.

When we varied the mesh size, we observed that the strain profile near the interface is inversely dependent on the distance from the surface. By analogy with gas dynamics, we refer to this region of strain localization as a boundary layer. In gas dynamics, the gas is assumed to stick to the surface over which the bulk material is flowing. The strain-rate dependent shear strength (viscosity) results in a boundary layer characteristic thickness that depends on the free stream velocity and the viscosity. For our rate independent calculation, the power varies between 0.6 and 0.9, depending on the radial location. This inverse dependence is observed both by fitting the profile of each calculation after the plastic strain field has reached its final state and by fitting the peak value achieved in each calculation as a function of the original (square) mesh size in the range 20 to 100 microns. We note that inverse (first-power) distance dependence was observed by Liu [13] in Eulerian simulations of spigot and Steven tests using a constant yield stress. In the Eulerian framework, no interface slip is permitted. In our simulations the power law is about the same, whether using a friction coefficient of 0.4, or a higher value that prevents slip (> 0.577). We show the vertical plastic strain profile in Figure 5 at a time when the plastic strain field has reached its final state, at a radial coordinate that is 2/3 the original radius, where the mesh was observed to stick. In summary, friction at the interfaces leads to a strong localization of shear strain at an intermediate radius, and also near the outer periphery of the disk on conical surfaces that intersect the corners of the disk. Figure 6 illustrates the plastic strain distribution for a friction coefficient of 0.4.

Some researchers [8] have advocated limiting the frictional resistance on the surface to be the shear strength of the weaker material, in contrast to the assumptions of gas dynamics. Instead of severe localization of strain near the interface, this technique essentially replaces a boundary layer of extreme distortion with additional energy being

dissipated at the interface. As others have done, we limited the frictional shear stress to be that of the shear stress at yield, 115 MPa. The results are given in Table 1. In the LS-DYNA simulations that limit the frictional stress, to a good approximation the additional surface energy is accompanied by an equal reduction in the plastic shear strain energy in the boundary layer. Although energy conservation is good, the unaccounted energy was systematically greater for those calculations that limited the shear resistance. We note that in LS-DYNA the energy absorbed in hourglass resistance is normally not counted, and that there was more significant hourglass distortion for the calculations that limited shear.

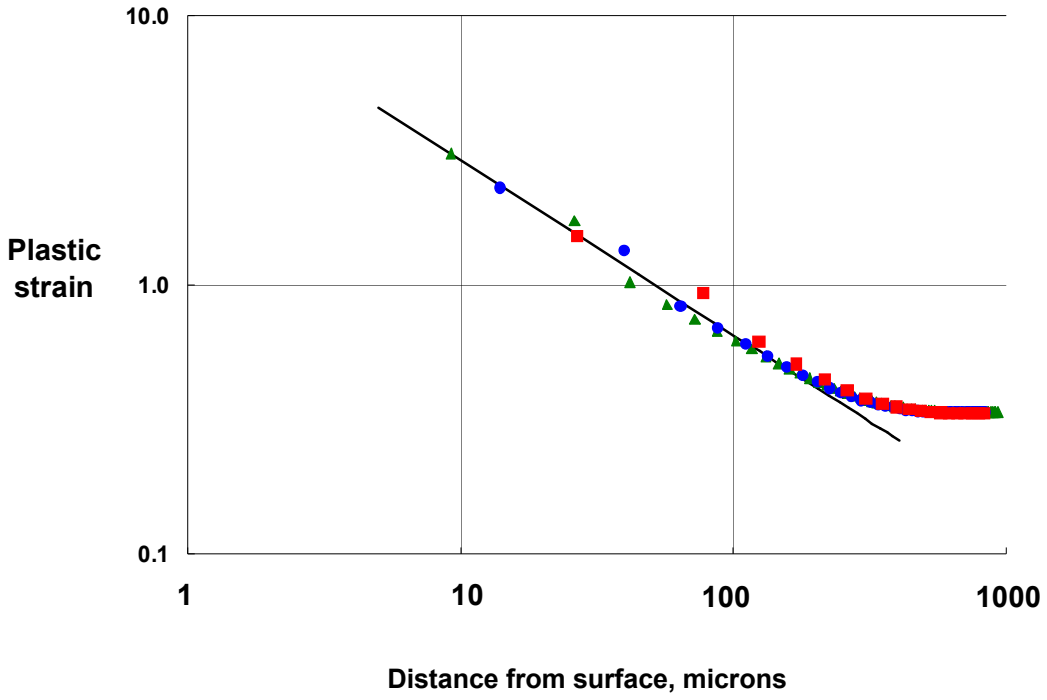

Figure 5. Plastic strain as a function of vertical distance from the interface at a fixed radius of 0.33 cm for initial mesh sizes 20 (green triangle) 31 (blue circle) and 62 (red square) microns. The fitted line has an inverse 0.65 power. Calculations used constant yield strength and no limit to the frictional forces, and are shown at 0.45 milliseconds.

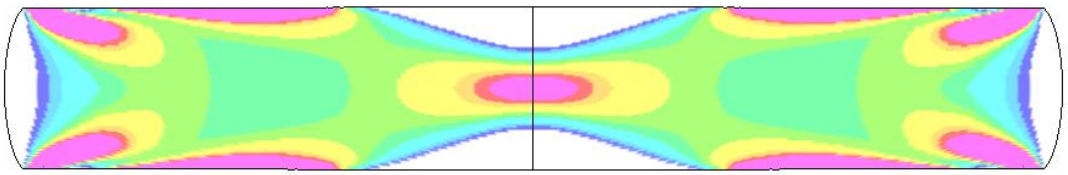

Figure 6. The plastic strain distribution is from a calculation with constant yield stress and no limit to the frictional forces. Plastic strains greater than 0.5 are shown as magenta and plastic strains less than 0.2 are uncolored. The values increase from blue through green and yellow to red (rainbow fringe plot). The vertical line is the axis of symmetry of the disk. The time is 0.45 milliseconds, just as the drop hammer begins to rebound. Original mesh size was 31 microns. The strain localization in the center of the disk has peak value 0.6. The strain localizations near the surface at radius between 2.2 and 4.5 mm, and near the corners have peak values over 2.

An earlier phenomenological ignition criterion for the Steven Test [14] was based on frictional work at the interface. Our criterion is based on the localization of shear strain, weighted by the normal stress. Both criteria are strongly affected by friction. Both ignition criteria also bypass the calculation of the temperature field, so do not directly represent a time-at-temperature criterion that would be consistent with temperature-driven decomposition kinetics. The analyses of Ball [14] do incorporate the calculation of the temperature field to change the shear strength of the adjacent materials.

Table 1. Effect of limiting the maximum frictional shear stress. Initial drop hammer kinetic energy is 20.908 J.

Mesh size, microns	Limiting shear stress, MPa	Internal energy, J	Surface energy, J	Rebound kinetic energy of striker, J	Unaccounted energy, J
62.5	unlimited	15.435	3.085	2.364	0.024
62.5	110	13.798	4.897	2.134	0.078
62.5	115	13.986	4.718	2.125	0.078
62.5	120	14.234	4.585	2.009	0.080
31.3	unlimited	15.803	2.721	2.375	0.009
31.3	115	13.930	4.685	2.252	0.041

Since the HERMES model already includes parameters to quantify how increasing the ambient temperature reduces the effective strain rate, it would seem a natural extension to incorporate dynamic temperature effects. To calculate the reduction of strength near the interface requires a dynamic calculation of the temperature profile, including the heat gained from frictional work on the surface, and the heat lost to the adjacent steel. In contrast to metals, explosive crystals and the binders used in explosive formulations are very poor thermal conductors, with thermal diffusivity two to three orders of magnitude less than that of typical metals. If we use a nominal value of 0.001 cm^2/s for the thermal diffusivity, and use as a characteristic time 0.2 millisecond, which is appropriate for both US and UK variants of the Steven test (and by coincidence our

drop hammer geometry) the characteristic distance affected by thermal diffusion is 5 microns. At this length scale plastic-bonded explosives are not continua. The explosive crystal bimodal size distribution in terms of mass fraction per logarithmic diameter bin in many explosive formulations includes the characteristic thermal distance. The coarse fraction of the crystallites is centered near 100 microns and the fine fraction centered at 5 to 10 microns. The distributions are broad, with a full-width at half maximum spanning 0.4 to 2.5 times the diameter at the peak. In the bulk of the material, the binder thickness is typically in the range 0.1 to 0.5 microns, depending on the volume fraction of binder and the specific surface area of the explosive crystals. Near the surface of the explosive part, the composition can be binder rich if it is molded or pressed into shape. If the part is machined to shape, if may have the nominal composition if the explosive crystals and binder are cut cleanly, or be binder rich if the machining process spreads the soft binder over the cut crystal faces, or have extra defects if crystallites are pulled out of the binder matrix. Finally, the surface roughness of the machined steel confinement is also in this range. As a result, further investigation in this aspect of ignition is probably best accomplished using mesoscale simulations to examine both the structural reorganization of the crystallites after substantial shear deformation, the conduction of heat thorough the steel interface and explosive boundary layer, and the effective reduction of the shear strength of the composite explosive with temperature. We expect that the binder strength and the strength of the assembly of explosive crystals will show different response to increasing temperature.

When the shear stress is limited, the plastic strain distribution in the boundary layer is exponential, rather than hyperbolic. (See Fig.7) Limiting the frictional stress to the shear strength has a beneficial effect in that the calculated strain field is much less localized, and the mesh is consequently much more regular. Reduced localization is also observed when we incorporate strain hardening. (See Figure 8.) For those calculations, the strain hardening is linear, and increases the strength to 220 MPa at a logarithmic strain of one. The results of a sequence of calculations with different coefficients of friction are given in Table 2. Note that neither the internal energy absorbed by the disk, nor the surface energy dissipated is monotonic in the friction coefficient. This latter effect can be understood as the competition between increased slip distance and reduced force that results when the friction coefficient is reduced. As a result, we have used the nominal logarithmic thickness strain, which is uniform as a function of radius, to estimate effective friction coefficients when the frictional retarding stress is limited. We note that for both zero friction, and the condition for sticking (friction coefficient > 0.577), we would expect the surface energy to be zero. In the calculations, the surface energy given by LS-DYNA is slightly greater than zero. For the case of a large friction coefficient, we noted that the surface energy increases only during unloading when the drop hammer is rebounding. For the case of zero friction, we speculate that the surface energy is not zero because the local surface is not perfectly flat, so there is a contribution from the normal stress.

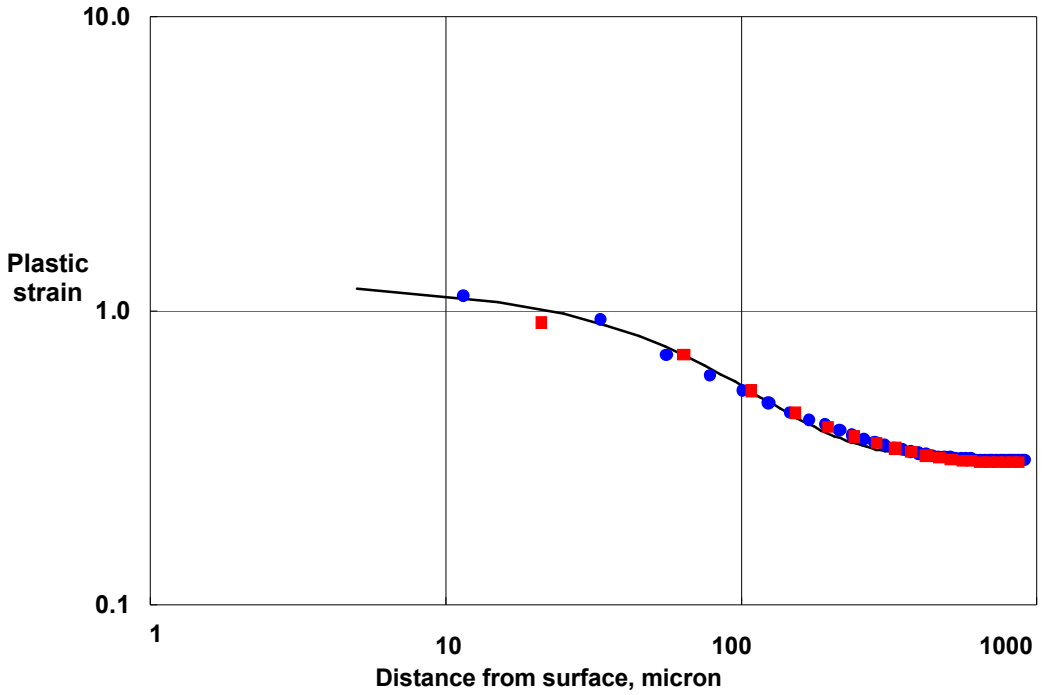

Figure 7. Plastic strain distribution at 0.45 milliseconds for calculations with constant yield stress and the frictional stress limited to 115 MPa. Mesh sizes are 62 microns (red squares) and 31 microns (blue circles). They are shown with a fitted exponential curve with characteristic length 73 microns.

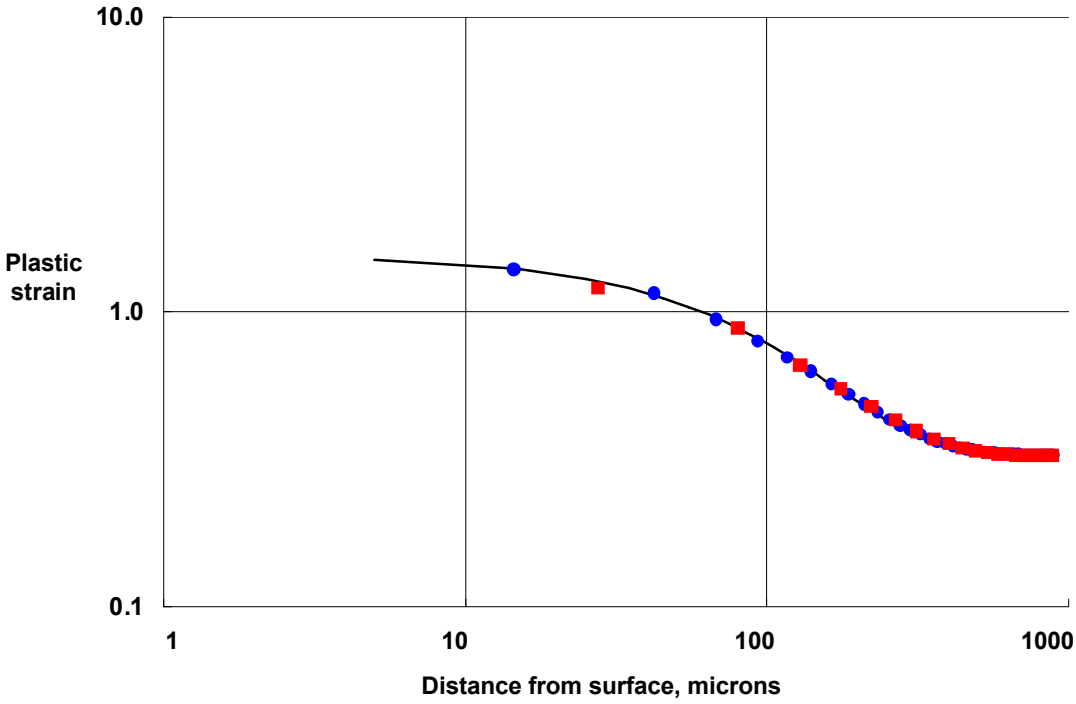

Figure 8. Strain localization near the interface for a calculation with friction coefficient 0.4, and incorporating strain hardening. Mesh sizes are 62 microns (red squares) and 31 microns (blue circles). The fitted exponential curve has a characteristic length of 100 microns.

Table 2. Summary of results for various coefficients of friction with no limit set on the frictional stress. Initial striker kinetic energy is 20.91 J. Strength includes strain hardening.

Friction coefficient	Sample internal energy, J	Striker rebound kinetic energy, J	Surface energy dissipated, J	Thickness strain
0	19.62	1.14	0.13	0.492
0.1	16.00	1.40	3.48	0.393
0.18	14.21	1.82	4.86	0.332
0.25	13.66	2.10	5.12	0.294
0.28	13.73	2.20	4.96	0.282
0.33	14.15	2.34	4.38	0.267
0.4	15.14	2.53	3.21	0.254
0.9	17.64	2.89	0.35	0.246

The axial stress at the upper and lower interfaces depends on the radius, and has its maximum at the axis of symmetry. The axial stress profile on the lower interface is shown in Figure 9 at various times in the simulation. To a good approximation, the axial stresses on the lower and upper surfaces are the same. The moving platen begins to reverse its velocity at about 0.5 msec. The peak value of the axial stress on axis depends on the friction coefficient. When the friction coefficient is zero, the axial stress is uniform and takes the value of the yield stress. This extra stress is not a dynamic effect. We performed one calculation with the mass of the platens increased 100 fold, and the velocity reduced 10 fold. For the case with friction coefficient equal 0.4, the peak axial stress was 785.2 MPa, compared with the value obtained at the nominal velocity of 784.9 MPa. We then performed three additional calculations with the friction coefficient 0.4, but with the resisting stress limited to 50, 90, and 120 MPa. Results of these calculations are given in Table 3.

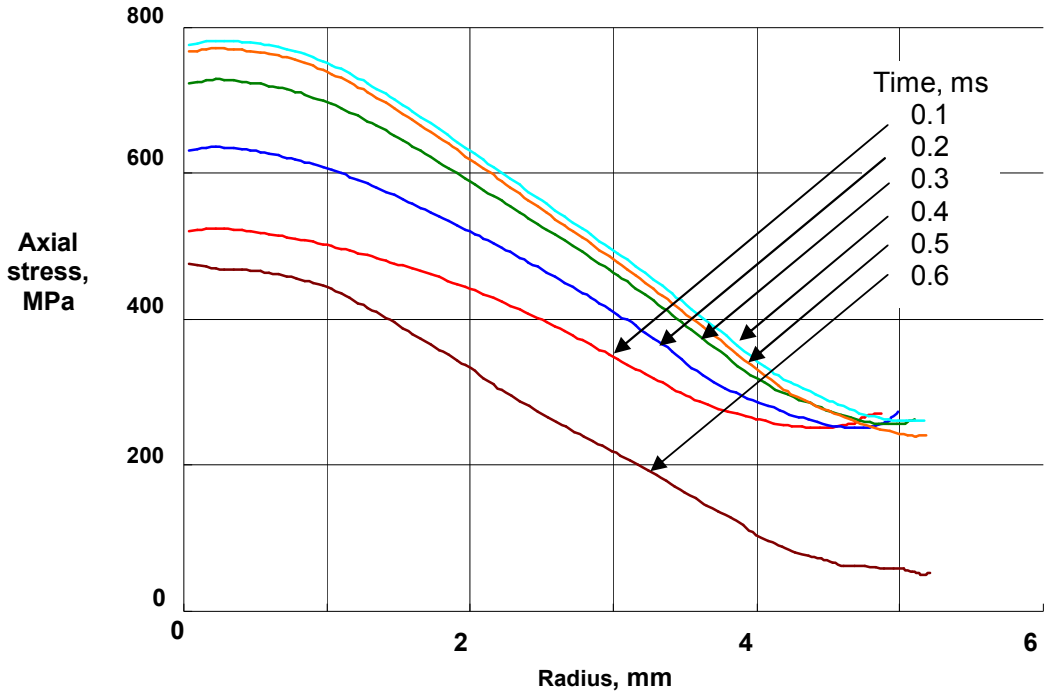

Figure 9. Axial stress is shown as a function of radius at various times during the calculation. The friction coefficient was 0.4 with no limit to the frictional stress. The mesh size was 31 microns. The drop hammer reverses its velocity between 0.4 and 0.5 ms, and the sample begins to unload.

Table 3. Summary of results for various values of the limiting stress. The equivalent coefficient of friction is based on the thickness strain.

Limit stress, MPa	Sample internal energy, J	Striker rebound kinetic energy, J	Surface energy dissipated, J	Thickness strain	Equivalent friction coefficient
50	14.08	1.73	5.02	0.341	0.16
90	13.38	2.10	5.34	0.285	0.29
120	13.88	2.25	4.70	0.272	0.33

The combination of high friction coefficient (or perfect sticking in Eulerian simulations) and constant yield stress results in plastic strain or heating from plastic work that varies inversely with distance from the interface. As a result, an ignition criterion based on plastic strain such as ours will exhibit severe mesh-size dependence. This can be finessed to an extent by incorporating the mesh size in the criterion. Experience with similar extrapolations when calculating the initiation of fracture suggests that unanticipated and unphysical ignitions should be anticipated. We suggest treating all such extrapolated ignitions as numerical artifacts until proven otherwise.

An ignition criterion based on frictional work at the interface is only possible with a Lagrange formulation of the sliding interface. Even so, the partition between the surface energy and the plastic work that develops in the adjacent elements depends on the friction

coefficient and the decision to limit or not to limit frictional resistance by the shear stress of the weaker material. We note that a strain-rate dependence of the shear strength adds much complication to the simple idea of limiting the frictional resistance. Since we wish to apply our ignition criterion to Eulerian as well as Lagrange simulations, we reject ignition criteria based on frictional work.

The use of either rate-dependent strength or strain hardening (or both) has been seen to reduce the mesh-size dependence of the strain distribution. In our simulations described above, the characteristic distance for the strain distribution was on the order 100 μm. This dimension results in a feasible resolution requirement for simulations of research test vehicles, and may be feasible in other geometries as well.

We emphasize that our ignition criterion is a phenomenological one. We wish to let the localization of shear strain indicate likely locations for ignition, and obtain the value of the ignition parameter by simulating a research test vehicle geometry at the observed ignition threshold. As a result, our criterion lacks a time-at-temperature dependence. It is possible that ignition tests performed at either much smaller or much larger scale would illustrate the need for a more complete criterion. Until such experimental results are available, we have deferred complicating our criterion. We do suggest caution when applying the model at much larger scale, where the consequences of ignition are more hazardous.

7. Calculation of pressure and energy density using the entropy

Calculations that incorporate the pressure equilibrium method described in [2] were observed to give poor estimates of the gas pressure and temperature when there is a small mass fraction of gas present. Eulerian and ALE simulations are also known to exhibit this effect in mixed cells with small amounts of gas. Even though the volume change of an element may be small, most of that change is taken up by the small mass of gas present. As a result, the gas volume change is very large. The standard method to calculate the gas adiabat is only accurate when the magnitude of the volume change is less than about 5% [15]. In expansion, the energy change is overestimated so the gas cools to an unphysical low temperature.

We sought a method that would substantially improve the accuracy without resorting to expensive subcycling. Our strategy is to use the entropy directly as a way to solve for the specific energy density and pressure at the end of a hydrodynamic calculational step. In order to examine alternative numerical strategies it is convenient to start with material descriptions for which the entropy and other thermodynamic potentials are analytic functions. In the simplest case, consider the orthotropic gas. For that case the pressure, p, is given as a function of specific volume, v, and temperature, T by

$$p = \frac{\omega C_v T}{v}, \tag{36}$$

Where ω is the adiabatic exponent (γ-1) and C_v is the (constant) specific heat at constant volume. The change in internal energy density is given by

$$de = \left.\frac{\partial e}{\partial v}\right)_T dv + \left.\frac{\partial e}{\partial T}\right)_v dT\,. \tag{37}$$

Substituting the standard thermodynamic derivatives,

$$de = \left[-p + T\frac{\partial p}{\partial T}\right)_v \right] dv + C_v dT \,. \tag{38}$$

The result of integration is,

$$e = e_0 + C_v (T - T_0)\,, \tag{39}$$

where the 0 subscripts refer to the initial condition. Similarly, for the change of entropy, *s*,

$$ds = \frac{\partial s}{\partial v}\Big)_T dv + \frac{\partial s}{\partial T}\Big)_v dT \tag{40}$$

and with thermodynamic substitutions,

$$ds = \frac{\partial p}{\partial T}\Big)_v dv + \frac{C_v}{T} dT\,, \tag{41}$$

so that

$$s = s_0 + \omega C_v \ln\frac{v}{v_0} + C_v \ln\frac{T}{T_0}\,. \tag{42}$$

The linear solid is only slightly more complicated. Here

$$p = p_0 + K\left(\frac{v_0}{v} - 1\right) + \frac{\omega C_v}{v}(T - T_0)\,, \tag{43}$$

where *K* is the bulk modulus. By similar manipulation,

$$e = e_0 + C_v (T - T_0) + (K - p_0)(v - v_0) - (Kv_0 - \omega C_v T_0)\ln\frac{v}{v_0} \tag{44}$$

and

$$s = s_0 + \omega C_v \ln\frac{v}{v_0} + C_v \ln\frac{T}{T_0} \tag{45}$$

We assume a mixture of solid and gas, with the mass fraction of gas, λ, fixed. For a given change in volume of the mixture, we solve for pressure equilibrium by Newton iteration. With a starting assumption that all the volume change is taken up by the gas, with the physical constraint that there is some volume remaining for the solid when the mixture is in compression, we solve for the new energy density and pressure during each iteration step.

For a given new value of volume, we calculate the temperature at the old value of entropy by inverting equation (42) for the gas or (45) for the solid. We calculate the new pressure and energy density using equations (36) and (39) for the gas, or equations (43) and (44) for the solid. The iteration for gas-solid pressure equilibrium and gas-solid insolubility

$$v = \lambda v_{gas} + (1 - \lambda) v_{solid} \tag{46}$$

is continued until satisfactory agreement in pressure obtained. For the case where there is no artificial viscosity, the entropy does not change.

We find the correct solution by using the standard 2-step pressure-energy iteration [2], which is used in many hydrocodes, but taken to the limit of small volume change by subcycling. We tested our result for the case where the logarithmic change in volume in one step is 1.0 (new specific volume of the element is 2.718 times the old. The new

method is exact. We compare the results for a specific case where the gas fraction is 0.2 in Table 4.

Table 4. Comparison of new method and standard method for the case of no artificial viscosity

	P, MPa	V, cc/g	Vs	Es, J/g	Ts, K	Vg	Eg	Tg
Starting values	200	0.92937	0.49505	-23.38	300	2.6667	-4093	2000
Correct	25.103	2.5263	0.49854	-23.78	297.9	10.637	-4626	1001.4
New method	25.103	2.5263	0.49854	-23.78	297.9	10.637	-4626	1001.4
Two-step	17.315	2.5263	0.49869	-23.71	297.8	10.637	-4792	690.66

For the case of artificial viscosity, the increase in entropy must be calculated accurately, or the newly proposed method is no better than the original two-step iteration. We found that if we added the energy density increment due to artificial viscosity to the energy density at the old time, then calculated the new entropy, and updated the temperature, energy density, and pressure we got an answer that was too high in pressure. If on the other hand, we calculated the energy density at the new volume using the old value of entropy, then add the heating from artificial viscosity, and calculate the new temperature, entropy, and pressure, the result was too small in pressure. We chose the expedient of using the average of the entropy calculated in these two ways. The result for the same volume increment and an artificial viscosity of 10 MPa is shown in Table 5.

Table 5. Comparison of new method and standard method for the case of +10 MPa artificial viscosity

	P, MPa	V, cc/g	Vs	Es, J/g	Ts, K	Vg	Eg	Tg
Starting values	200	0.92937	0.49505	-23.38	300	2.6667	-4093	2000
Correct	22.189	2.5263	0.49859	-23.82	297.9	10.637	-4688	885.11
New method	22.273	2.5263	0.49859	-23.82	297.9	10.637	-4686	888.47
Two-step	14.271	2.5263	0.49875	-23.74	297.8	10.636	-4856	569.24

We examined the effect of a larger value of the artificial viscosity. For purposes of illustration we have assumed a compressive artificial viscosity for volume expansion, which occurs in numerical simulations when quadratic artificial viscosity is used in both expansion and compression. For this larger viscosity, there is substantial cooling during expansion. For the larger entropy change, the new method has larger error, but remains much smaller than the two-step iteration. See Table 6.

Table 6. Comparison of new method and standard method for the case of +50 MPa artificial viscosity

	P, MPa	V, cc/g	Vs	Es, J/g	Ts, K	Vg	Eg	Tg
Starting values	200	0.92937	0.49505	-23.38	300	2.6667	-4093	2000
Correct	10.533	2.5263	0.49883	-23.97	297.7	10.636	-4936	420.12
New method	10.014	2.5263	0.49859	-23.82	297.7	10.636	-4947	399.41
Two-step	2.0968	2.5263	0.49899	-23.93	297.6	10.636	-5115	83.627

Since the new method is also a two-step iteration, there is a considerable gain in accuracy for the small extra expense of evaluating the entropy.

8. Calculation of entropy for other equations of state

At present our use of HERMES has been in circumstances where the rates of reaction and pressure increase is modest. As result, the peak pressures have only been small multiples of the confinement strength. The temperature rise in the unreacted explosive has been small, since the relatively low pressures are achieved by a loading path that is more nearly adiabatic than a shock Hugoniot. As a result, the equation of state for the reactant needed accuracy for off-Hugoniot states, but not necessarily for high pressures or temperatures. In our test of the entropy method (Section 7) we considered only simple equation of state forms, and constants for the thermomechanical properties. Our proposed method to change the way in which energy density and pressure are calculated, must have general applicability. Indeed, our intent to extend the HERMES model to include the possibility of DDT (Deflagration to detonation transition) and XDT (now understood to involve the recompression of explosive fragments) will require more general forms where constant properties are not appropriate.

Examples for unreacted explosive include the form proposed by Lambourn [16] for explosive formulations, or that proposed by Sewell and Menikoff [17] for the explosive itself. In those cases, which include variable specific heat that approaches a limit at high temperature, the entropy can be expressed as functions of specific volume and temperature, but neither form is analytically invertible in terms of either temperature or energy density. One possibility is to select forms for the specific heat that permit analytic inversion. The other options for minimal extra computational expense are fitting the inverse function by an analytic function and preparing a tabular function as an adjunct to an analytical equation of state. An extra cost option is numerical inversion, which would require iteration. In principle, having the analytic derivatives available could speed convergence of such iteration.

In HERMES, we are using a tabular equation of state to represent the gas products. We attempted to construct the entropy function on that table by using the interpolation functions to evaluate the derivatives in Equation 41, and construct the entropy over each square represented by density (or specific volume) and temperature increments. We found that with close spacing in the table, we could construct an entropy

density surface that was nearly path independent. With a table spacing that was otherwise adequate to represent the $p(v,T)$ and $e(v,T)$ surfaces, the calculations were substantially path dependent. Since tables are generally constructed by a method that is based on the free energy, and uses derivatives of that free energy to evaluate the thermodynamic properties, it is easier and more accurate to simply add an entropy surface to the pressure and energy density surfaces. We note that when the equation of state surface represents a changing (equilibrium) composition, the entropy density has a component due to the composition. When we constructed a table at fixed composition, in the limit of small tabular intervals our construction method was reasonably accurate. With changing composition, our pseudentropy did not have the same value as the entropy, but adiabats calculated with either entropy or pseudo entropy were nearly the same. In any case, our calculation of pseudoentropy is made more difficult by the limited number of significant digits that are routinely available in the table. With very close spacing, the derivatives are inaccurate because they are based on taking the difference of two large numbers.

9. References

1. J.E. Reaugh, *Progress in model development to quantify High Explosive Violent Response (HEVR) to mechanical insult*, LLNL report LLNL-TR-405903, August 1, 2008.
2. J.E. Reaugh, *Calculating the Dynamics of High Explosive Violent Response (HEVR) after Ignition*, LLNL report LLNL-TR-407915, October 20, 2008.
3. J.E. Reaugh, *Implementation of Strength and Burn Models for Plastic-bonded Explosives and Propellants*, LLNL report LLNL-TR-412938, May 2009.
4. J.E. Reaugh and A.G. Jones, "Mechanical Damage, Ignition, and Burn: Experiment, Model Development, and Computer Simulations to Study High-Explosive Violent Response (HEVR)," in *Proceedings, 14th International Symposium on Detonation*, Coeur d'Alene, ID, April 2010. (In press)
5. O. Vorobiev, "Generic strength model for dry jointed rock masses," *International Journal of Plasticity,* **24**, p2221, 2008.
6. M.L. Wilkins, R. D. Streit, J. E. Reaugh, *Cumulative-Strain-Damage Model of Ductile Fracture: Simulation and Prediction of Engineering Fracture Tests*, LLNL report UCRL-53058, Livermore, CA, October 3, 1983.
7. M.L. Wilkins, *Computer Simulation of Dynamic Phenomena*, Springer, 1999.
8. R.E. Winter, G.J. Ball, and P.T. Keightley, "Mechanisms of Shock-induced Dynamic Friction," *J. Phys D: Appl. Phys.* **39**, p5043, 2006.
9. W. Schroeder and D.A. Webster, "Press-forging thin sections: effect of friction, area, and thickness on pressure required," *J. Appl. Mechanics – Trans. ASME*, **16**, (3), p289, 1949.
10. D.J. Steinberg, *Equation of State and Strength Properties of Selected Materials*, LLNL report UCRL-MA-106439 Change 1, February 13, 1996.
11. P.J. Rae and D.M. Dattelbaum, "The properties of poly(tetrafluoroethylene) (PTFE) in compression," *Polymer*, **45**, p7615-7625, 2004.
12. D.M. Hoffman and J.B. Chandler, "Aspects of the Tribology of the Plastic Bonded Explosive LX-04," *Propellants, Explosives, and Pyrotechnics*, **29**, 2004, p368.
13. Ben Liu, private communication, LLNL, September 2009.

14. S.K. Chidester, L.G. Green, and C.G. Lee, "A frictional work predictive method for the initiation of solid high explosives from low pressure impacts," *10th Detonation Symp. (Int.)*, Boston MA, 1993, p785.
15. D.J. Andrews, private communication, Physics International Corporation, ca 1968.
16. B.D. Lambourn, "A Complete EOS for Non-reacted Explosive," *Shock Compression in Condensed Matter 2005*, AIP 845, 2006, p165.
17. T.D. Sewell and R. Menikoff, "Complete Equation of State for β-HMX and implications for initiation," *Shock Compression in Condensed Matter 2003*, AIP 706, 2004, p157.